

Low-dose X-ray CT simulation from an available higher-dose scan

Masoud Elhamiasl & Johan Nuyts

KU Leuven, Department of Imaging and Pathology, Nuclear Medicine & Molecular Imaging, B-3000 Leuven, Belgium

E-mail: masoud.elhamiasl@kuleuven.be, johan.nuyts@uzleuven.be

Abstract. In CT-imaging an optimal compromise between the radiation burden and the image quality for the imaging task is needed. Lower-dose CT is desirable, however, lowering the dose results in a lower signal-to-noise ratio and therefore in a reduced image quality. In this research, we aim to develop a tool to simulate lower-dose scans from an existing standard-dose scan. The main application of this tool is to determine the lowest possible radiation dose that still produces sufficient clinical information. The X-ray tube current reduction is modeled by estimating the noise equivalent number of photons in the high exposure scan and applying a thinning technique to reduce that number. The proposed method accounts for the bowtie filter, for the electronic system noise, for the noise correlation between neighboring detector elements, for the beam hardening effect, and for the non-linear smoothing filter in very low dose scans. Several phantom studies with different acquisition protocols were performed to evaluate the accuracy of the proposed framework. The results demonstrate a close agreement between the noise magnitude and texture of the measured and the simulated lower-dose scans. For instance, the standard deviation of noise in the simulation of lower-dose scans with 90% tube current reduction matches the reconstructions from the real scans with less than 1% and 3% error for sequential and helical scans, respectively. The noise texture was also assessed by analyzing the noise power spectrum of the simulated lower-dose images which matches those from the real scans. Furthermore, the relation between the measured and predicted noise in projection domain is very close to the line of identity which confirms the accuracy of the model.

Keywords: dose reduction, low-dose simulation, X-ray computed tomography, computer simulation, noise modeling, protocol optimization.

1. Introduction

Computed tomography (CT) is one of the most commonly used imaging modalities for diagnosis, treatment planning, and patient follow-up. The number of CT examinations is still increasing due to excellent soft tissue resolution (contrast), high spatial resolution, and short acquisition duration. However, there are some concerns regarding the risks associated with ionizing radiation exposure to the patients. Various measures have been

taken to keep the dose as low as reasonably achievable (ALARA). Furthermore, modern CT scanners have been equipped with different components to minimize unnecessary radiation to the patient including bowtie filter, automatic exposure control (AEC), and also raw data preprocessing and advanced reconstruction algorithms in combination with lowering the tube current.

Low-dose CT scans can be achieved by reducing the radiation exposure to the patient, i.e. by lowering the X-ray tube current. However, there is a compromise between the radiation burden and the image quality in the imaging task. Lowering the radiation results in a lower signal-to-noise ratio and therefore in a poorer image quality. The most common way to determine the lowest possible radiation dose in CT protocols is clinical evaluation by physicians (Singh et al. 2009, Guimarães et al. 2010, Sollmann et al. 2019, Cros et al. 2017, Mittone et al. 2014). One method is to perform repeated scans with different radiation levels on the same patient and select the lowest exposure scan with minimum acceptable information. This strategy, however, is not ethical due to multiple exposures of the patient or should be done on phantoms instead where its clinical relevance is less. A more sophisticated strategy is to develop a tool to simulate reduced-dose scans from an existing high exposure scan and determine the lowest exposure scan which still provides sufficient information for the clinical task.

Dose reduction simulation techniques can be classified into two categories: those based on reconstructed CT images and those based on projection data. The methods of both categories simulate the lower dose scans by adding a proper synthetic noise to the higher-dose scan. The first approaches add noise in image space without the usage of the transmission data (Won Kim & Kim 2014, Kim & Kim 2012, Wang et al. 2012, Neverauskiene et al. 2018). These approaches are especially effective when the raw projection data are not available. However, nonlocal noise properties in reconstructed CT images (Massoumzadeh et al. 2009) make it very difficult to simulate noise directly in the image domain. In the absence of raw projection data, an alternative way can be to generate a virtual sinogram from a high dose CT image (Naziroglu et al. 2017, Takenaga et al. 2016) and model dose reduction in the sinogram domain.

The methods of the second category simulate lower-dose scans by adding synthetic noise to the higher dose scan in the projection domain. Our method falls into the second category. The existence of appropriate noise models in projection space is the main advantage of this category. The methods of this category mainly use a monochromatic noise model and consider synthetic noise as a Poisson, normal, or combination of Poisson and normal distribution. A detailed analysis of the transmission signal statistics was proposed by Whiting (Whiting 2002, Whiting et al. 2006) and Nuyts (Nuyts et al. 2013).

Preliminary works on dose reduction simulation have been done by Mayo (Mayo et al. 1997) and Frush (Frush et al. 2002) by adding random Gaussian noise to the high exposure projection data. However, the effect of electronic noise was ignored in their model. Shortly afterward, Amir (Amir et al. 2003) used projection data to estimate the variance of synthetic Gaussian noise and added the reconstructed noise to the high dose scan in image space. Previous studies have shown that the bowtie filter and tube

current modulation are two components that significantly affect the noise characteristics of CT transmission data. Massoumzadeh (Massoumzadeh et al. 2005, Massoumzadeh et al. 2009) and Yu (Yu et al. 2012) simulated the lower-dose scan by including the effects of electronic noise, bowtie filter, and tube current modulation in the simulation. The electronic noise obeyed a zero-mean Gaussian distribution and the noise in the higher dose scan was included in their models. Zabic (Žabić et al. 2013) used a realistic non-Gaussian electronic noise which was measured during no-X-ray scans on the real systems to improve the accuracy of the simulations in very low dose scans. This model also accounted for the fact that the high dose scan was already noisy. Zeng (Zeng et al. 2015) investigated the relationship between the incident flux of low and high dose scans and proposed a simple tool for low dose simulation by considering the effect of both quantum and electronic noise. Wang (Wang & Pelc 2011*b*, Wang & Pelc 2011*a*) proposed a model similar to Frush (Frush et al. 2002) for dual-energy CT data with the goal of simulating data with various tube voltages.

In the state-of-the-art approaches, the transmitted data is often considered as the combination of Poisson and normal distribution (Zeng et al. 2015, Žabić et al. 2013, Benson & De Man 2010, Ma et al. 2012, Rong et al. 2017) which is a good approximation of CT transmitted data. Additionally, the noise was often considered to be spatially uncorrelated although the noise of neighboring detector channels is actually correlated due to crosstalk between detector elements (Whiting et al. 2006, Willemink et al. 2018, Abadi et al. 2018). It is worth noting that the noise propagation through the image reconstruction is not the same for correlated and uncorrelated noise, therefore, this correlation should be included in the simulation procedure. The uncorrelated noise does not exhibit the correct noise texture and results in the underestimation of the real noise magnitude in lower-dose scans (Wang et al. 2014). Wang (Wang et al. 2014) assumed the noise to be spatially correlated where the correlation was introduced by convolving the uncorrelated white noise with a kernel. The injected correlated noise accounted for both quantum and electronic noise, as well as their spatial correlation.

In this research, we aim to develop and validate a dose reduction simulation tool to simulate lower-dose CT scans from an existing standard-dose scan. The main motivation is to determine the lowest possible radiation dose that still produces sufficient information for proton therapy treatment planning. However, this paper focuses on the issue of low dose CT simulation with a first evaluation based on the noise characteristics. Its application in proton therapy is ongoing research and will be reported on in future publications. The bowtie filter, the electrical noise, the crosstalk between detector channels, the beam hardening effect, and the non-linear smoothing filter in very low dose scans have been included in the proposed model. The proposed method employs the binomial distribution for thinning the high dose scan, which accounts for the fact that the higher exposure scan is already noisy. Most of the effects accounted for in our method have also been considered in previous publications, but to our knowledge, a method simulating all these effects was not previously proposed. In particular, many existing methods do not model the detector cross-talk and the non-linear smoothing

filter. The preliminary results on a water phantom have been published at Fully3D 2019 conference (Elhamiasl & Nuyts 2019).

The rest of this paper is organized as follows. A brief review of X-ray CT noise is presented in Sec. 2.1 and this section is followed by the proposed method for lower-dose CT scan simulation. Experimental results are described and discussed in Sec. 3, and finally, some concluding remarks are drawn in Sec. 4.

2. Methodology

Lower-dose CT scans can be modeled by adding a proper synthetic noise to a higher dose scan. In this section, the noise model of X-ray CT will be described and the effect of each CT scanner component on the noise model will be investigated in more detail. A new framework will then be developed to simulate lower-dose scans by estimating the noise equivalent number of photons in the higher exposure scan and applying a thinning technique to reduce that number.

2.1. Noise model

An X-ray tube produces polyenergetic X-rays, with a distribution of energies which depends on the applied tube potential and inherent filtration (Whiting et al. 2006). Additionally, at a fixed tube voltage, the number of X-ray photons emitted from an X-ray tube depends on the product of the tube current and the exposure time. In the rest of the paper we will refer to this product as the *tube load*. It has commonly been assumed that the incident X-ray intensity with the tube load α , $I_0^{(\alpha)}$, is linearly proportional to the tube load and its value depends on the tube current, the measurement duration time, and bowtie filter.

A CT scan is a set of measurements I_i , which are produced by photons passing through the patient body along a given ray path i , denoted by $l(i)$. Passing through the patient, the incident X-ray beam is attenuated by random absorption and scattering events. The I_i then enters the energy integrating detector and gets converted into an electronic signal. For polyenergetic X-rays generation, it is convenient to assume that $I_0^{(\alpha)}$ is grouped into discrete energy bins E_m , $m = 1, \dots, M$, with probabilities λ_m . The values of λ_m spatially vary due to the effect of the bowtie filter and heel effect (La Riviere 2005). The mean number of surviving photons \bar{I}_m of energy E_m arriving at the detector unabsorbed and unscattered can be described by Beers law

$$\bar{I}_m = I_0 \lambda_m \exp \left(- \int_{l(i)} \mu(x, E_m) dx \right) \quad (1)$$

where $\mu(x, E_m)$ represents the energy-dependent attenuation map. In practice, the recorded value I_m is corrupted by many sources of variability and the real value of it is not available (Nuyts et al. 2013). The noise produced in the detectors consists of quantum noise and electronic noise, and unless the attenuation along the path is extremely high, it is dominated by the former. The quantum noise is due to the limited

number of X-ray photons detected by the detector and can be well modeled as a Poisson distribution. The detectors also add additional variability to the recorded signal, called electronic noise, due to fluctuations in the electronic components. The electronic noise is dominated by readout noise, which is independent of the exposure time, and we assume it obeys a normal distribution. In modern CT systems, the mean value of the electronic noise is measured before each scan in a short no-X-ray scan and the calculated mean is subtracted from the scan data. Consequently, the electronic noise can be modeled as a zero-mean normal distribution. The total number of photons of energy E_m that arrives at the detector can be written as

$$I_m = \mathcal{P}(\bar{I}_m) + \mathcal{N}(0, \sigma_e^2) \quad (2)$$

where $\mathcal{P}(a)$ denotes a realization of a Poisson distribution with mean a and $\mathcal{N}(0, \sigma^2)$ represents a realization of a zero-mean normal distribution with variance σ^2 . This means that for a polychromatic X-ray generator, the CT transmission data I_i , observed in detector element i , can be modeled as a combination of a compound Poisson distribution and a normal distribution (Whiting et al. 2006). The contribution of each detected photon in the measured detector signal is proportional to its energy E_m . Consequently, we can assume that each detected signal is a realization of a random variable I_i whose statistics are described by

$$I_i = G_i \sum_{m=1}^M E_m \mathcal{P}\left\{ I_{0i} \lambda_m e^{-\int_{l(i)} \mu(x, E_m) dx} \right\} + \mathcal{N}\{0, \sigma_e^2\} \quad (3)$$

where G_i represents detector conversion factor (La Riviere 2005). The first term in Eq. 3 represents the effect of photon statistics, an energy-weighted combination of Poisson random variables which results in compound Poisson statistic (Whiting 2002, Elbakri & Fessler 2003), and the second term represents the influence of the electronic noise.

Even though the proposed model in Eq. 3 can describe the polychromatic nature of X-ray generation, it is inconveniently complicated. To simplify Eq. 3, we can start by approximating a compound Poisson distribution as a (scaled) Poisson distribution which can be written as

$$I_i = \sum_{m=1}^M w_m I_m = \sum_{m=1}^M w_m \mathcal{P}(\bar{I}_m) \simeq \omega \mathcal{P}(\bar{I}_\omega) \quad (4)$$

where ω and \bar{I}_ω are fitting parameters. The quantity \bar{I}_ω can be regarded as the noise equivalent count of the original (compound Poisson distributed) signal (Strother et al. 1990). The fitting parameters can be determined by requiring that the mean and variance of the Poisson distribution equal that of the compound Poisson distribution, which means

$$\sum_{m=1}^M w_m I_m = \omega \bar{I}_\omega \quad (5)$$

$$\sum_{m=1}^M w_m^2 I_m = \omega^2 \bar{I}_\omega \quad (6)$$

Note that if the tube load of the CT scanner is increased, all I_m increase by the same factor, and therefore \bar{I}_ω has to be increased by the same factor too. Thus, \bar{I}_ω is proportional to the tube load, and ω accounts for the weights introduced by the energy spectrum and the detector characteristics. Consequently, we can simplify Eq. 3 by approximating the compound Poisson distribution as a simple Poisson distribution and use a monochromatic attenuation line integral. This approximation gives us

$$I_i \approx G_i \bar{E}_i \mathcal{P} \left\{ I_{0i} e^{- \int_{l(i)} \mu(x, \bar{E}) dx} \right\} + \mathcal{N}\{0, \sigma_e^2\} \quad (7)$$

where \bar{E}_i represents average energy. In addition, we can assume that this scaling factor, $G_i \bar{E}_i$, is the same for an air scan and a transmission scan. In the proposed method, the scaling factor vanishes since we always use the ratio of an air scan and a transmission scan. For simplicity, in the rest of the paper, we drop the subscript i , unless it is important to indicate it.

2.2. Quantifying the incident x-ray intensity

Dose reduction can be modeled by estimating the (noise equivalent) number of photons in the high exposure scan and applying a thinning technique to it. Assuming a monochromatic beam, the mean number of detected photons in the high dose scan of β mAs can be written as

$$I^{(\beta)} = \beta I_0^{(1)} \exp(-\rho) \quad (8)$$

where ρ denotes log-converted data. For the scanners considered in our project, the raw data contain log-converted data, $\rho = \ln(I_0/I)$. The log-converted raw data should first be converted into the form of transmission data using Eq. 8 which requires knowledge of $I_0^{(1)}$, a noise free estimate of the incident X-ray intensity for a unit tube load. At a fixed exposure time, the X-ray intensity is linearly proportional to the tube current which means $I_0^{(\alpha)} = \alpha I_0^{(1)}$ where α represents the tube current (Wang et al. 2008). The variance of an air scan without any attenuating object can be used to estimate the incident X-ray intensity for every detector element. Modeling the transmission data as a combination of a Poisson and a normal distribution, the variance of the transmission data in an air scan is given by

$$\text{var} \left[\exp(-\rho_{air}^{(\alpha)}) \right] = \text{var} \left[\frac{I_{air}^{(\alpha)}}{I_0^{(\alpha)}} \right] = \frac{\text{var}[I_{air}^{(\alpha)}]}{(I_0^{(\alpha)})^2} = \frac{\alpha I_0^{(1)} + \sigma_e^2}{(\alpha I_0^{(1)})^2} \quad (9)$$

Performing some air scans at different levels of tube load, the system is overdetermined and $I_0^{(1)}$ and σ_e^2 can be estimated using a least square estimator. When the number of incident photons $\beta I_0^{(1)}$ is known, the number of surviving photons in the transmission scan can be estimated with Eq. 8.

2.3. Thinning technique

Knowing the number of surviving photons in a high-dose scan with tube load β mAs, our goal is to simulate a lower-dose scan of α mAs. A thinning technique can be applied

on the surviving photons of the high-dose scan to produce a (more) noisy low-dose scan. Thinning means the random elimination of some of the detected photons with survival probability of α/β , where the chance of not being eliminated is the same for each photon. Thinning of a known number of counts n with survival probability p produces a binomial distribution $\mathcal{B}(n; p)$. Employing a binomial distribution for thinning accounts for the fact that the higher-dose scan is also noisy.

The thinning should be applied to the quantum noise and not on the electronic noise, but there is no easy way to separate the two contributions for a single, noisy measurement. Therefore, we apply the shifted Poisson approximation (Yavuz & Fessler 1998) to Eq. 2 as follows:

$$I_m = \mathcal{P}(\bar{I}_m) + \mathcal{N}(0, \sigma_e^2) \simeq \mathcal{P}(\bar{I}_m + \sigma_e^2) - \sigma_e^2 \quad (10)$$

where σ_e^2 is the mean electronic noise contribution (this is a known constant, unaffected by noise). Both distributions have the same mean and variance, they differ only in the higher order moments. With this approximation, the total noise (including both quantum and electronic noise) on the signal is expressed as an effective number of photons and becomes amenable for thinning. However, the thinning also reduces the contribution of the electronic noise, whereas in reality, the electronic noise contribution is independent of the tube load. Therefore, that contribution is restored by adding a (noisy) number of additional photons. After the thinning, the mean electronic noise is subtracted to restore the correct mean, as in Eq. 10. This leads to

$$I_{sim}^{(\alpha)} = \mathcal{B}\left(\beta I_0^{(1)} \exp(-\rho) + \sigma_e^2, \frac{\alpha}{\beta}\right) + \mathcal{P}\left\{(1 - \frac{\alpha}{\beta})\sigma_e^2\right\} - \sigma_e^2 \quad (11)$$

The first term reduces the number of photons observed in the converted raw transmission data, which itself is a random value because ρ is obtained from a measurement. The electronic noise is modeled as additional photons, which are also thinned. The second term adds a noisy number of photons to compensate for the thinning of the electronic noise. The last term subtracts the mean number of electronic noise photons, to ensure that the electronic noise has zero mean.

2.4. Noise correlation

So far, it is assumed that the noise contribution of any detector element is independent of that of the other detectors. Turning to the experimental evidence, we found that the noise of neighboring CT detector pixels is correlated with an almost fixed correlation matrix r which is due to crosstalk between detector pixels (Whiting et al. 2006). Considering that CT detectors are very small compared to the human body, we can assume that neighboring detectors i and j see the same intensity \bar{A} , such that their covariance can be written $C_{ij} = r_{ij}\bar{A}$, where r_{ij} is the noise correlation. The covariance between the detector pixels i and j is decreased to $\eta^2 C_{ij}$ after applying the thinning algorithm with survival probability of η . The problem is that in realistic data, the covariance should equal ηC_{ij} , not $\eta^2 C_{ij}$. This problem emerges due to the fact that

during the thinning, we ignore the fact that neighboring detectors sometimes see the same photons. Since two independent thinning samples were generated from that single contribution, the correlation is suppressed.

It is important to restore this noise correlation in the lower-dose simulated scan because the noise propagation through the image reconstruction is not the same for correlated and uncorrelated noise. Therefore, we have to create an additional covariance of $(\eta - \eta^2)C_{ij}$, without changing the mean or the variance of the noise, and also without changing the correlations in the data, which should be correctly inherited from the original high count data.

The thinning noise N_i , defined as the difference between the signal after thinning and the signal before thinning scaled with η , is an uncorrelated zero-mean noise, satisfying

$$\text{var}[N_i] = \eta \bar{A}(1 - \eta) \quad (12)$$

which follows from the fact that thinning produces samples from a binomial distribution. Here, the idea is to convolve that thinning noise with a convolution mask w to restore the correlation between detector pixels. Convolving N_i with a convolution mask w generates the samples Q_i :

$$Q_i = \sum_j w_{i-j} N_j \quad \forall_k \quad w_k = w_{-k} \quad \text{and} \quad w_k \geq 0 \quad (13)$$

The random variables Q_i have the following features:

$$\bar{Q}_i = \sum_j w_{i-j} \bar{N}_j = 0 \quad (14)$$

$$\begin{aligned} \text{var}[Q_i] &= \mathbb{E}[Q_i^2] = \mathbb{E}\left[\sum_j \sum_k w_{i-j} w_{i-k} N_j N_k\right] \\ &= \sum_j w_{i-j}^2 \mathbb{E}[N_j^2] = \sum_j w_{i-j}^2 \text{var}[N_j] \\ &= \eta \bar{A}(1 - \eta) \sum_j w_j^2 \end{aligned} \quad (15)$$

$$\begin{aligned} \text{cov}[Q_i, Q_j] &= \mathbb{E}[Q_i Q_j] = \mathbb{E}\left[\sum_k w_{i-k} N_k \sum_{k'} w_{j-k'} N_{k'}\right] \\ &= \sum_k \sum_{k'} w_{i-k} w_{j-k'} \mathbb{E}[N_k N_{k'}] = \sum_k w_{i-k} w_{j-k} \mathbb{E}[N_k^2] \\ &= \eta \bar{A}(1 - \eta) \sum_k w_{i-k} w_{j-k} = \eta \bar{A}(1 - \eta) \sum_\xi w_\xi w_{i-j-\xi} \\ &= \eta \bar{A}(1 - \eta) [w \otimes w]_{i-j} \end{aligned} \quad (16)$$

where $\mathbb{E}[N_j N_{k \neq j}] = 0$ because the thinning noise is uncorrelated. The last equation is obtained by setting $\xi = k - i$ and using $w_{-\xi} = w_\xi$. It can be concluded that smoothing the thinning noise with mask w has no effect on the mean, scales the variance by a factor $\sum_j w_j^2$, and introduces a covariance which equals the convolution of the mask with itself

and multiplied with the variance of the original thinning noise. Therefore, combining Eq. 12 and Eq. 16, the additional covariance created by convolving thinning noise with the convolution mask w should satisfy:

$$\eta \bar{A} (1 - \eta) [w \otimes w]_{i-j} = (\eta - \eta^2) r_{ij} \bar{A} \quad (17)$$

Consequently,

$$[w \otimes w]_{i-j} = r_{ij} \quad (18)$$

The correlation matrix r can be obtained by performing a blank scan and estimating the correlation between neighboring detector pixels at a large number of locations (many independent noise realizations). The convolution in Eq. 18 can be then written as the multiplication of two circulant matrices and convolution mask w can be computed as the square root of matrix r .

2.5. Beam hardening effect

So far, the relation between beam intensity and the effective number of photons has been derived using blank scans. However, in patient scans, the photon beams reaching the detector are harder than in blank scans, because of the beam hardening effect. A harder beam contains fewer photons for the same intensity and is therefore subject to a higher amount of quantum noise (Whiting et al. 2006).

In order to estimate the compensation ratio, two signals which produce the same beam intensity were generated. The first signal was decreased by water attenuation while the second signal was decreased by reducing the tube load. The beam hardening compensation ratio is given by the ratio of the variance of the signal reduced by the tube load to the variance of the signal reduced by water attenuation. Mathematically, it can be written as:

$$\text{Scaling Factor} = \frac{\sum_m S E_m^2 I_m}{\sum_m E_m^2 I_m \exp(-\mu_m l)} \quad (19)$$

where I_m is the beam intensity, E_m is the energy bin and, $\exp(-\mu_m l)$ represents water attenuation at energy E_m . The numerator and the denominator represent the variance of the signal reduced by the tube load and water attenuation, respectively. The parameter S was set to obtain the same intensity for both signals.

Knowing the attenuation value and bowtie thickness in each beam path (and therefore its effect on the energy spectrum), and assuming that all patient attenuation is due to water (Benson & De Man 2010), the true value of the effective number of surviving photons can be predicted by multiplying the number of surviving photons in Eq. 8 by the scaling factor in Eq. 19. Fig. 1 represents the compensation ratio for different values of water and Teflon (bowtie) attenuation. It can be observed that the beam hardening effect is not negligible, for example, beam hardening by 20 cm of water produces 11 percent more variance than that of an air scan with the same intensity for an energy spectrum with 120 kVp, a tungsten anode, and typical filtering.

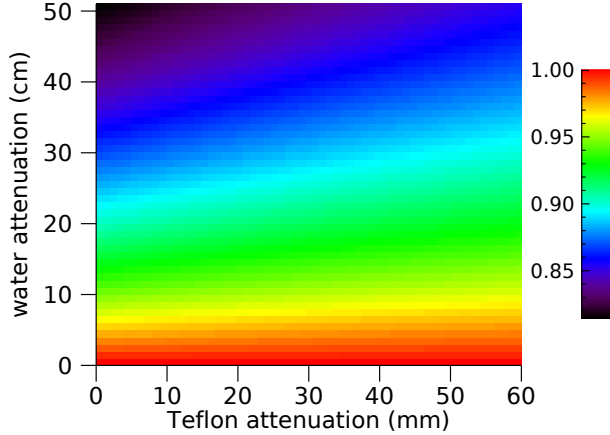


Figure 1: This figure represents the ratio of the variance of the signal reduced by the tube load to the variance of the signal reduced by water attenuation.

2.6. Signal dependent filter

The CT scanners are usually equipped with a preprocessing software, such as a low pass filter (Yu et al. 2012), to avoid negative values to be passed to the log when the detected signal is very small. In agreement with this, we observed that the noise level in very low-dose scans was less than predicted. Not knowing the vendor algorithm, we designed a signal dependent filter (SDF) by requiring that, when the number of photons is below a particular threshold, the noise to signal ratio, NSR, no longer increases with decreasing number of photons. As a consequence, the correlation between neighboring pixels increases when this filter is applied. The number of photons for which the filter must be activated was determined by analyzing the correlation between neighboring pixels.

The principle of the SDF is to smooth the detected signal by a simple 3×3 smoothing filter and mix the smoothed, \bar{x}_i , and the non-smoothed, x_i , signals according to the value of the smoothed signal. The combination of the smoothed and non-smoothed signal for the detector element i , \tilde{x}_i , can be described as follows

$$\begin{aligned} \tilde{x}_i &= (1 - \tau)x_i + \frac{\tau}{n^2} \sum_{j=1}^{n^2} x_j \\ &= (1 - \tau + \frac{\tau}{n^2})x_i + \frac{\tau}{n^2} \sum_{j=1, j \neq i}^{n^2} x_j = \sum_{j=1}^{n^2} \gamma_j x_j \end{aligned} \quad (20)$$

where x_i represents the detected signal in pixel i , j is the index of neighborhood pixels, $n=3$ is the size of the smoothing matrix, and τ determines the combination ratio of the smoothed and non-smoothed signals. Here, the aim is to estimate γ to keep the NSR at a specific level when the detected signal is smaller than the smoothing threshold, T .

The NSR of the \tilde{x}_i is given by

$$\text{NSR} = \frac{\text{var}[\tilde{x}_i]}{\mathbb{E}[\tilde{x}_i]^2} = \frac{\sum_{j=1}^{n^2} \gamma_j^2 x_j}{\left[\sum_{j=1}^{n^2} \gamma_j x_j \right]^2} \quad (21)$$

When the detected signal is smaller than the smoothing threshold, the NSR of \tilde{x}_i should be similar to that of when $x_i = T$. Using $\sum_j \gamma_j = 1$, it follows that

$$\sum_{j=1}^{n^2} \gamma_j^2 \approx \frac{\bar{x}_i}{T} \quad (22)$$

where \bar{x}_i represents the signal smoothed by 3×3 averaging kernel. The corresponding value for τ is computed by combining Eq. 20 and Eq. 22. To sum up, the proposed framework estimates the equivalent number of photons in high dose scan and simulates the lower-dose scan by applying the thinning technique to that number. Subsequently, the simulated signal will be smoothed if it is smaller than the smoothing threshold.

So far, we described a model for sequential CT scans without automatic exposure control (AEC) where the tube load remains the same in all views. However, the model can be extended to the clinical helical scans with AEC by comparing the tube current of high and low dose scan for every single view. The lower-dose CT simulation procedure is described in Algorithm 1.

Algorithm 1 The procedure of lower-dose X-ray CT simulation.

Part 1: Parameter estimation

- 1: Perform blank scans at different tube loads.
- 2: Estimate the incident X-ray intensity, $I_0^{(1)}$, for each detector element and the variance of the electronic noise, σ_e^2 .

Part 2: Lower-dose scan simulation

- 3: Perform a high-dose scan.
 - 4: **for each** detector elements **do**
 - 5: Estimate the (noise equivalent) number of photons in high dose scan.
 - 6: Compensate the effect of beam hardening.
 - 7: Apply the thinning technique.
 - 8: **end for**
 - 9: Restore cross-talk correlation between neighboring detector elements.
 - 10: Compensate for electronic noise reduction due to thinning.
 - 11: Apply the SDF if the simulated signal is very small.
 - 12: Convert simulated transmitted signals to logarithmic space.
 - 13: Reconstruction.
-

3. Results

Several phantom studies were conducted to evaluate the performance of the proposed framework. In each experiment, a high-dose scan along with corresponding lower-dose scans were performed. The high-dose scan was used as an input to simulate the lower-dose scans according to the method given in section 2. The simulated scans were

Table 1: A detailed description of phantom studies. ρ denotes the log-converted measurement value as defined in Eq. 8.

Phantom	Scan Mode	AEC	Reconstruction	ρ range
21 cm water filled PMMA cylinder	sequential	No	MLTR	[-0.05, 4.51]
6 cm water filled PMMA cylinder	sequential	No	MLTR	[-0.17, 1.12]
Anthropomorphic thorax phantom	sequential	No	FDK	[-0.16, 7.00]
Anthropomorphic thorax phantom	helical	Yes	FDK	[-0.43, 7.25]
Anthropomorphic abdomen phantom	sequential	No	MLTR	[-0.14, 8.40]
Anthropomorphic head phantom	helical	Yes	vendor	[-0.43, 7.07]

then reconstructed and compared with corresponding real lower-dose acquired scans. The noise power spectrum (NPS) and the standard deviations of the reconstructed image in uniform ROIs were used for the comparison. Scans with different acquisition protocols, including sequential and helical scans, scans with AEC, and in-house or vendor reconstructions, were used to evaluate the robustness of the proposed strategy against different acquisition protocols. Table 1 provides the details of each experiment and the range of raw data in logarithmic space for each phantom.

All the scans have been acquired on a Siemens SOMATOM Force. The tube voltage was set at 120 kVp in all experiments. At each view, the X-ray projection covers a 2-dimensional detector area containing 920×96 detector pixels. Each scan contained 4 different sets where each set corresponds to one of the four possible focal spot positions. This Siemens scanner uses so-called Flying Focal Spot (FFS) to increase the transaxial and axial sampling and therefore the resolution of the system (Flohr et al. 2004, Flohr et al. 2005, Kachelrieß et al. 2006). The focal spot is moved forward and backward between two positions to increase the axial sampling (zFFS). For each of those positions, the focal spot is also moved from left to right to increase the transaxial sampling. Thus, the focal spot is moved to four different positions in four consecutive views and that affects the distance between the source and the detector. Since changing the distance between source and detector affects the photon flux, the four sets have been treated separately.

3.1. Parameter estimation

The incident X-ray intensity per unit tube load, $I_0^{(1)}$, and the variance of electronic noise, σ_e^2 , are the parameters to be estimated. The first step is therefore performing some air CT scans at different levels of tube load to calculate $I_0^{(1)}$ and σ_e^2 according to the method given in section 2.2. A total of seven different tube current levels, from 300 mAs down to 20 mAs, with the exposure time of 1 second were used and at each level the scans were repeated 5 times to compute the variance of the transmitted data for each detector element at each mAs level.

Turning to the experimental studies, we have noticed that some detector rows are

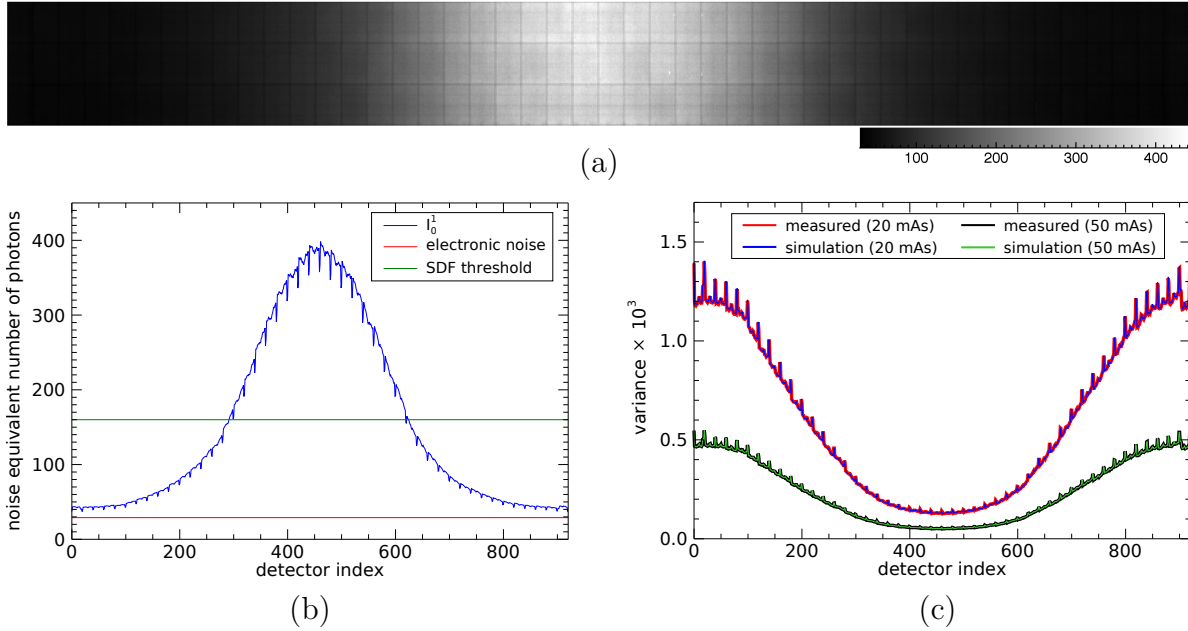


Figure 2: The illustration of the incident X-ray intensity per mAs (a) for all detector elements and (b) for a detector row (blue curve). The red and green lines in (b) show the variance of the electronic noise and the threshold where the SDF is applied for the Force scanner, respectively. (c) The comparison of the measured and the fitted variance of transmitted data in the blank scan of 20 and 50 mAs.

occasionally off by some arbitrary offset while the other rows in the same view are fine, which induces additional noise correlations. This offset does not have any effect on image reconstruction, but it significantly affects the variance of transmission data in the blank scan. To suppress this noise correlation, it can be assumed that the mean value of the acquired blank scan in each row remains the same and the transmission data should be normalized accordingly. This normalization results in a smaller variances on $\exp(-\rho)$ and therefore a larger $I_0^{(1)}$ as expected (see Eq. 9).

Fig. 2(a) is an image of the number of photons per mAs, $I_0^{(1)}$, for each individual detector pixel. It is an image of 920×96 pixels. The image reveals that the pixels are organized in 46×3 modules, each containing 20×32 detector elements. Fig. 2(b) represents the profile of $I_0^{(1)}$ and the variance of the electronic noise for one detector row. The bell shape profile of $I_0^{(1)}$ is due to the bowtie filter, which aims to reduce radiation dose to peripheral parts of the patient's cross-section, resulting in a non-uniform incident X-ray intensity. Because $I_0^{(1)}$ is determined for every detector element, the effect of the bowtie filter is automatically accounted for. It was assumed that the electronic noise was position independent with the same variance for all detector pixels. There are up to about 400 photons per unit mAs, the electronic noise is equivalent to 29 photons and the SDF threshold equals 160 photons. Fig. 2(c) illustrates the variance of the transmitted data for one detector row in the blank scan of 20 and 50 mAs and compares it with the fitted variance using estimated $I_0^{(1)}$ and σ_e^2 .

3.2. Simulation validation

In order to investigate the effect of each component on the simulation of lower-dose scans, four different models have been developed. The first model, the simplest one, simulates the lower-dose scan by applying the thinning to the number of surviving photons in the higher-dose scan and ignores the effect of beam hardening, the noise correlation and the SDF. Beam hardening has been included in the second model. The third model accounts for both beam hardening and noise correlation. The fourth model extends the third one by incorporating also the SDF.

In the first experiment, a water filled PMMA cylinder with diameter of 21 cm was scanned using sequential CT head-neck protocol. The lower-dose scans were simulated from a high-dose scan of 300 mAs and compared with corresponding acquired lower-dose scans. The scans were reconstructed using a maximum likelihood algorithm for transmission tomography (MLTR), applying 4 iterations and 25 subiterations (Van Slambrouck & Nuyts 2012) without applying any smoothing kernel. For a more detailed evaluation, the phantom was divided into central (C) and periphery (P) regions, represented in Fig. 5(a), and the standard deviation in each region was used for comparison. Fig. 3 compares the mean value of the noise standard deviation in the reconstructed images for each model at different levels of tube load. It is evident that decreasing the tube load increases the standard deviation in the reconstructed images. In addition, the standard deviation is not the same for center and periphery of phantom and the proposed model is able to track the noise levels for different regions.

For a better visualization, the standard deviation of the noise in each slice was normalized by the mean value of the standard deviation in the corresponding acquired lower-dose scan. Fig. 4 represents the normalized noise standard deviation for different models. Considering a correlated noise model, in contrast to previous studies, has increased the standard deviation in image space while it did not have any effect on the noise standard deviation in projection data. In addition, incorporating the effect of beam hardening along with noise correlation brings the noise value of the simulated image closer to the real low-dose image, except for the 20 mAs scan. In this scan, the signal intensity was very small and therefore a SDF filter was applied by the system to suppress the noise level. Consequently, the standard deviation of lower-dose real scans is found to be less than predicted. This error is more in the center of the phantom, Fig. 4(a), because the detected signal tends to be smaller due to higher attenuation in the center of phantom. However, when the SDF was included in the simulation, model 4 (final model), the reconstructed images of 20 mAs matches the reconstructions from the real data. Fig. 5 shows a high-dose scan of 300 mAs and its corresponding measured and simulated reduced-dose scans.

The noise texture in the reconstructed images was assessed by comparing the NPS in the real and simulated images. The NPS was computed by placing 13 squared ROIs of 51×51 voxel in the 20 slices. First, a 2D NPS was computed in the axial plane and then averaged over the planes. For better visualization, a 1D radially averaged

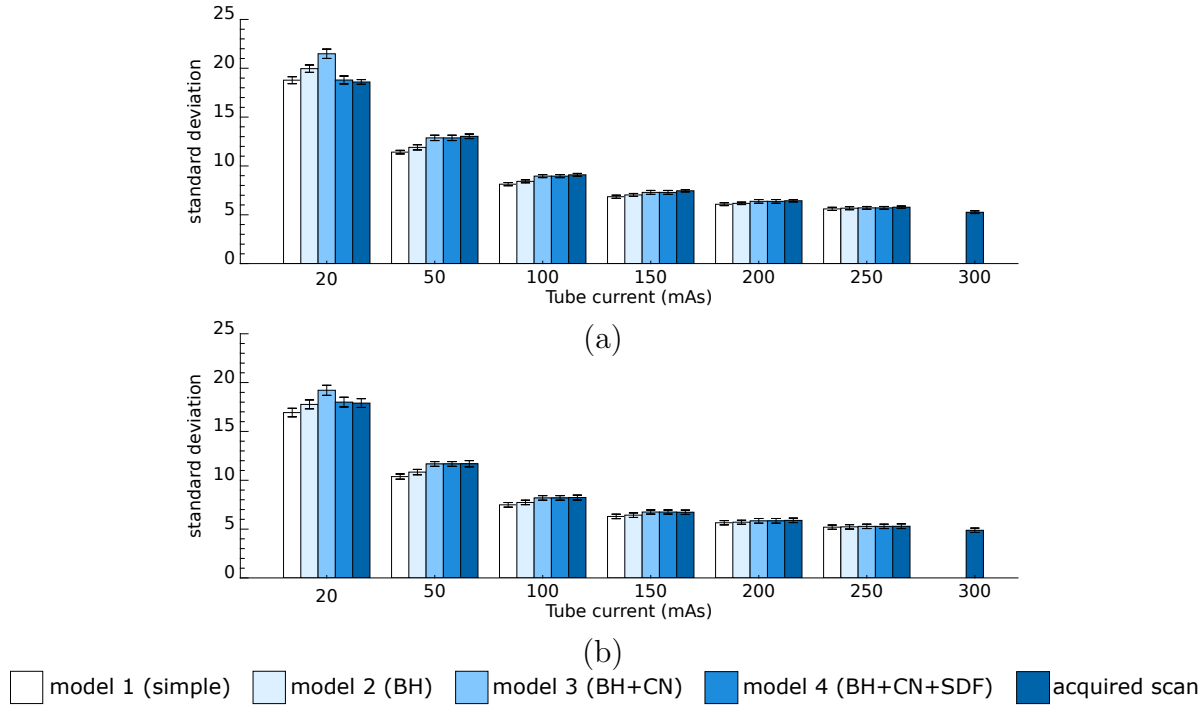


Figure 3: Representation of the standard deviation of the measured and the simulated images in the (a) center and (b) periphery of a 21 cm water phantom at different levels of tube current. The comparisons have been made between the models with different components, including beam hardening (BH), correlated noise (CN), and signal dependent filter (SDF). The error bars represent the variability of the noise in different slices.

profile of the 2D NPS was computed. Fig. 6 illustrates the NPS of simulated images and compares them with those of the real scans, confirming a strong agreement in the noise magnitude and texture between the measured and the simulated lower-dose scans.

As mentioned, the main limitation of model 3 arises when the number of detected photons is too small and a nonlinear smoothing filter is applied to suppress the image noise and therefore the variance of the acquired scan is found to be less than predicted. A new experiment has been designed to investigate the effect of this filter. The idea is to compare the simulated and real noise in the sinogram domain by subtracting two scans that have been taken at the same position. The difference between the two scans contains (almost) exclusively noise. The simulated noise is expected to be similar to that of the acquired one. Therefore, the aim is to estimate $\text{var}[\rho_{\text{sim}}^{(\alpha)} - \rho_{\text{real}}^{(\beta)}]$ and compare it with $\text{var}[\rho_{\text{real}}^{(\alpha)} - \rho_{\text{real}}^{(\beta)}]$ where $\rho^{(\alpha)}$ and $\rho^{(\beta)}$ indicate attenuation value of low and high dose scan, respectively. In order to compare the variances, the predicted variances were binned and for each bin the detectors associated with it were identified. For each bin, the variance of the measured signal over these detectors was computed. The variances from the measurements are compared to the predicted variances in Fig. 7. For the simulated scan of 20 mAs, the prediction computed without SDF deviated from the measurement for high variances, Fig. 7(a), shows that the variance of the simulated scan is higher than the acquired one before applying the SDF. Including the SDF in the simulation brought

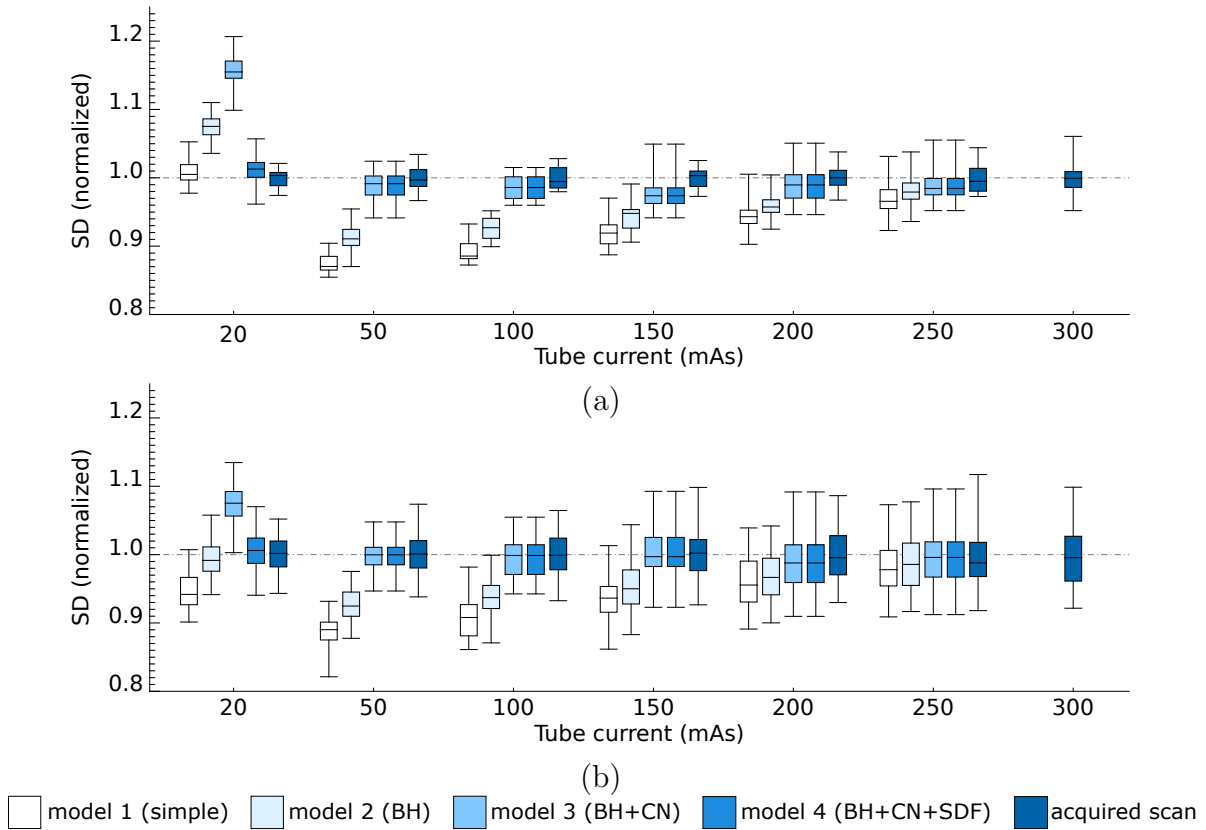


Figure 4: Comparison of noise level of reconstructed images in the (a) center and (b) periphery of a 21 cm water phantom at different levels of tube current. Incorporating the correlated noise (CN), beam hardening (BH), and signal dependent filter (SDF) brings the noise value of the simulated image closer to the real low-dose image. The error bars represent the variability of the noise in different slices.

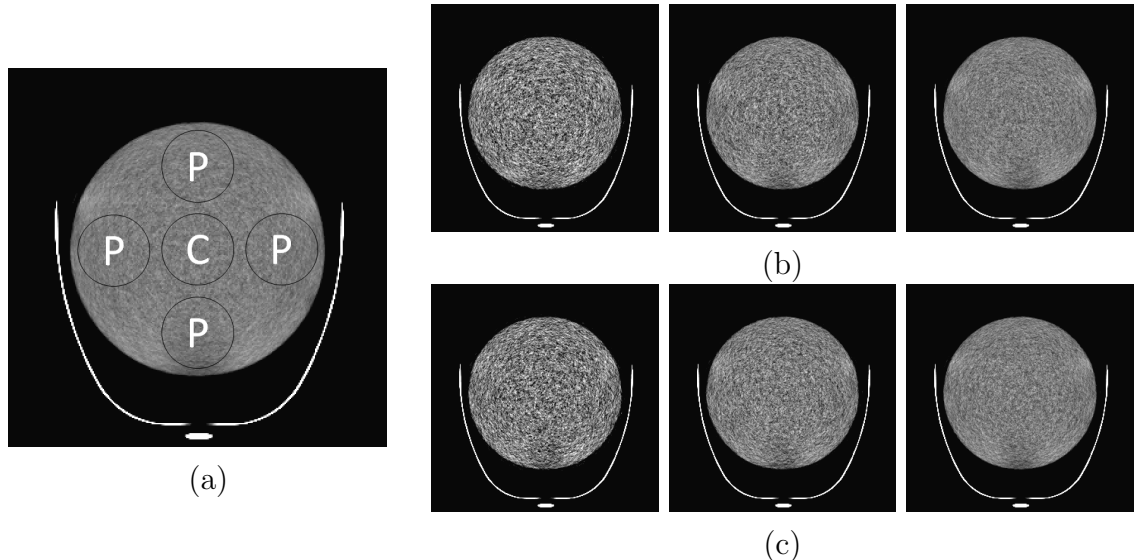


Figure 5: Presentation of (a) the measured high-dose image of 300 mAs, (b) corresponding acquired lower-dose images, and (c) simulated lower-dose images of 20, 50, and 100 mAs (from left to right) using the final model (window level: 0 HU, window width: 100 HU).

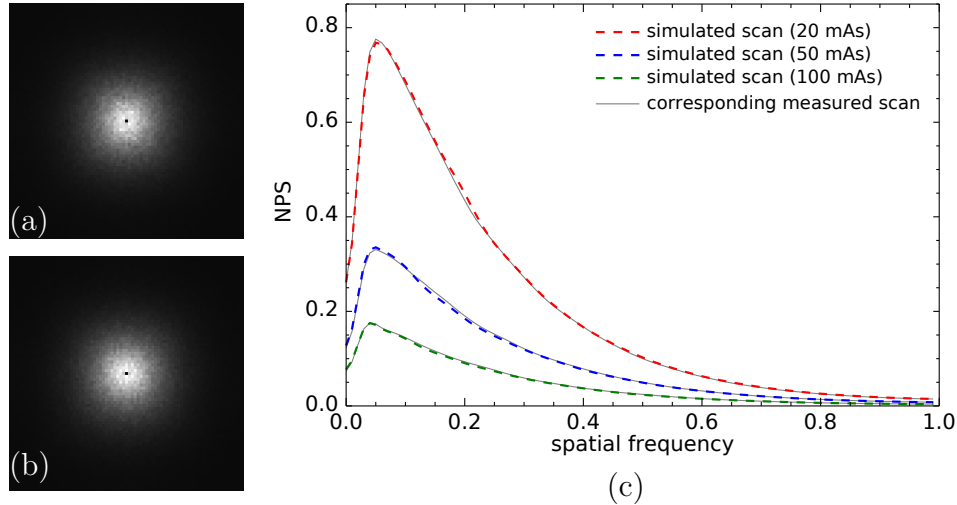


Figure 6: The illustration of the 2D NPS for (a) the measured and (b) the simulated scan of 20 mAs. (c) The comparison of radially averaged NPS for the measured and the simulated scans of 20, 50, 100 mAs.

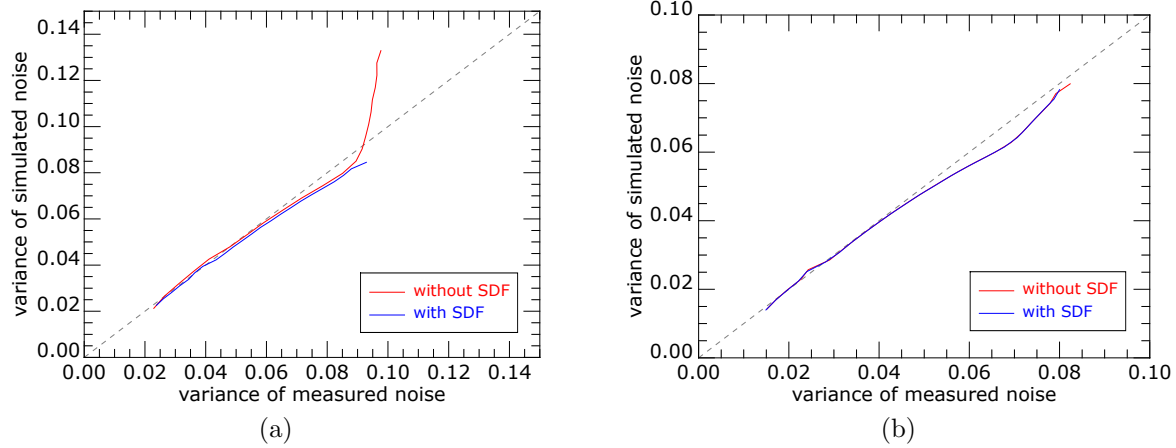


Figure 7: Comparison of the variance of the simulated noise versus acquired noise for the scan of (a) 20 mAs and (b) 50 mAs in the projection domain. The prediction deviates from the measurement for the scan of 20 mAs if the SDF has not been included in the simulation procedure.

the noise level much closer to the acquired noise (the blue curve Fig. 7). Fig. 7(b) compares the noise level of the simulated and the acquired scans of 50 mAs. For the higher dose scans, where the signal level is always higher than the smoothing threshold, applying the SDF does not have any effect on the simulation procedure and therefore the curve is very close to the line of identity for both models (with/without smoothing).

The same experiment was repeated for a small (6 cm diameter) water filled PMMA cylinder. For such a small object, the effect of beam hardening is less compared to the 21 cm phantom. A high-dose scan of 300 mAs was used and the lower-dose scans were simulated. Fig. 8 compares the standard deviation of the reconstructed images in the real and simulated lower-dose scans. Restoring the correlation increased the noise level

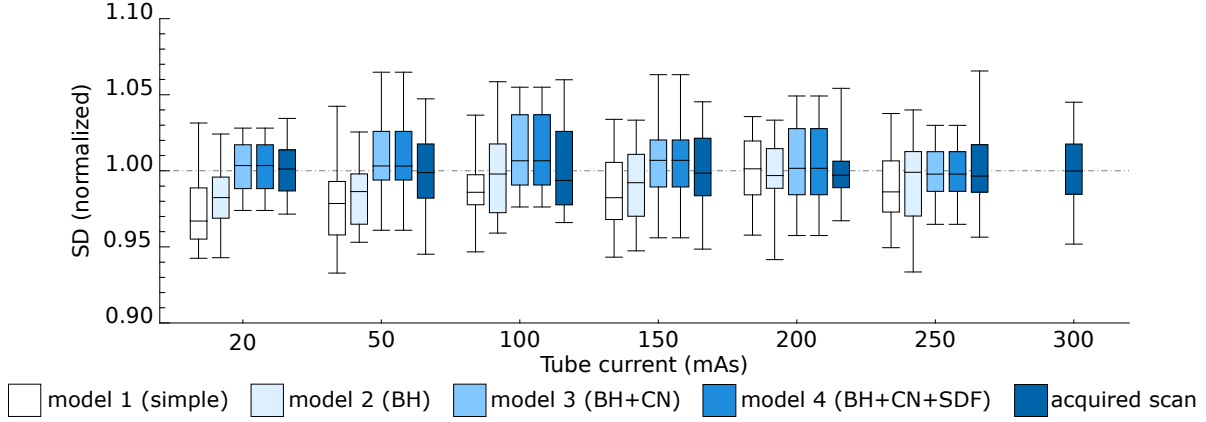


Figure 8: Presentation of the standard deviation of the reconstructed images of a 6 cm water phantom for different models at different levels of tube current.

Table 2: The detailed comparison of noise levels of the acquired and the simulated low-dose images at different levels of tube current for 21 cm and 6 cm water phantoms. The standard deviation of the noise in uniform ROIs were used for comparison.

Tube current	21 cm water phantom						6 cm water phantom		
	center			periphery			center		
	real	sim	error	real	sim	error	real	sim	error
300	5.25	-	- %	4.87	-	-	4.85	-	-
250	5.77	5.71	1.1%	5.29	5.28	0.2%	5.27	5.27	0.0%
200	6.43	6.37	0.9%	5.89	5.84	0.8%	5.77	5.80	0.4%
150	7.45	7.29	2.1%	6.72	6.74	0.2%	6.61	6.64	0.5%
100	9.09	8.95	1.5%	8.23	8.18	0.5%	7.95	8.05	1.1%
50	13.03	12.87	1.2%	11.69	11.67	0.1%	11.14	11.23	0.7%
20	18.59	18.79	1.0%	17.90	18.00	0.5%	17.67	17.70	0.1%

in image space; however, compensating beam hardening effect did not have significant impact on the results since the beam hardening is negligible for a 6 cm water phantom. In addition, the detected signal is always above the SDF threshold and therefore SDF did not have any effect on the simulated scans, consequently, the noise variance of model 2, 3, and 4 are almost the same.

Table 2 compares the standard deviation of the noise for the acquired and the simulated images of the first and second experiments. It reveals a close agreement in the observed and the simulated lower-dose scans. Accordingly, the relative error is less than 2.1% and 1.1% for 21 cm and 6 cm water phantoms, respectively, which confirms the accuracy of the proposed lower-dose simulation tool. For instance, the relative error is around 1% for the simulated scan of 20 mAs where the tube current was reduced by the factor of 15.

In the third experiment, an anthropomorphic thorax phantom (CIRS E2E SBRT) was analyzed by performing a sequential scan. The lower-dose scans were simulated from the scan of 300 mAs using model 4. The experiment was the same as the first

experiment but this time the FDK algorithm, without applying any smoothing kernel, was employed for the reconstruction. For the comparison, the phantom was divided into three regions, represented in Fig. 10(a), and the standard deviations in the uniform ROIs were compared. Fig. 9 compares the noise variance of the simulated and the acquired images. It can be seen that the proposed framework is able to model the noise for different regions at different levels of tube current. A detailed comparison between the simulated and the acquired images is presented in Table 3 where the relative error is less than 1.0%. Fig. 10 represents the simulated images and corresponding lower dose acquired images.

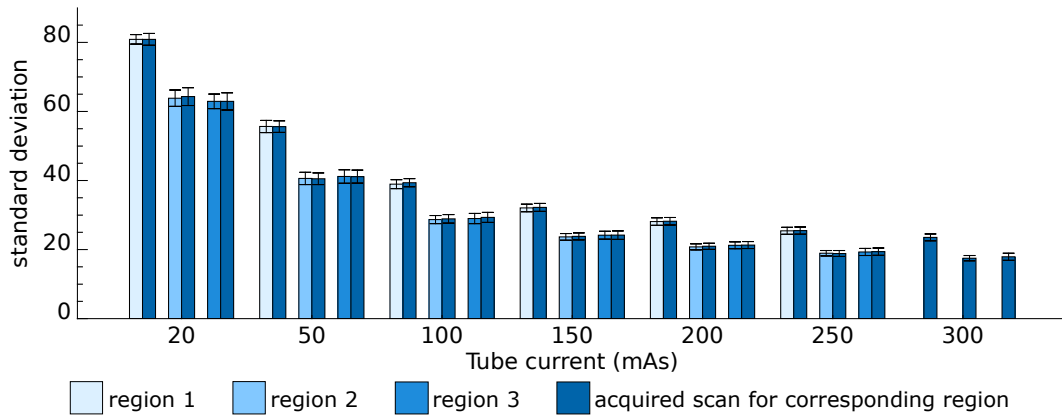


Figure 9: Comparison of the noise level of the simulated and measured images of an anthropomorphic thorax phantom for different regions at different levels of tube current.

Table 3: The detailed comparison of noise levels of the acquired and the simulated low-dose images for the sequential scan of the anthropomorphic thorax phantom.

Tube current	region 1			region 2			region 3		
	real	sim	error	real	sim	error	real	sim	error
300	23.54	-	-	17.51	-	-	17.92	-	-
250	25.50	25.44	0.2%	18.87	18.94	0.3%	19.40	19.30	0.4%
200	28.21	28.12	0.3%	20.96	20.78	0.8%	21.31	21.23	0.3%
150	32.22	32.06	0.5%	23.83	23.69	0.5%	24.18	24.17	0.0%
100	39.36	38.95	1.0%	28.89	28.69	0.7%	29.31	28.99	1.0%
50	55.61	55.65	0.06%	40.51	40.60	0.2%	41.13	41.17	1.0%
20	80.89	80.88	0.01%	64.31	63.84	0.7%	62.91	62.93	0.2%

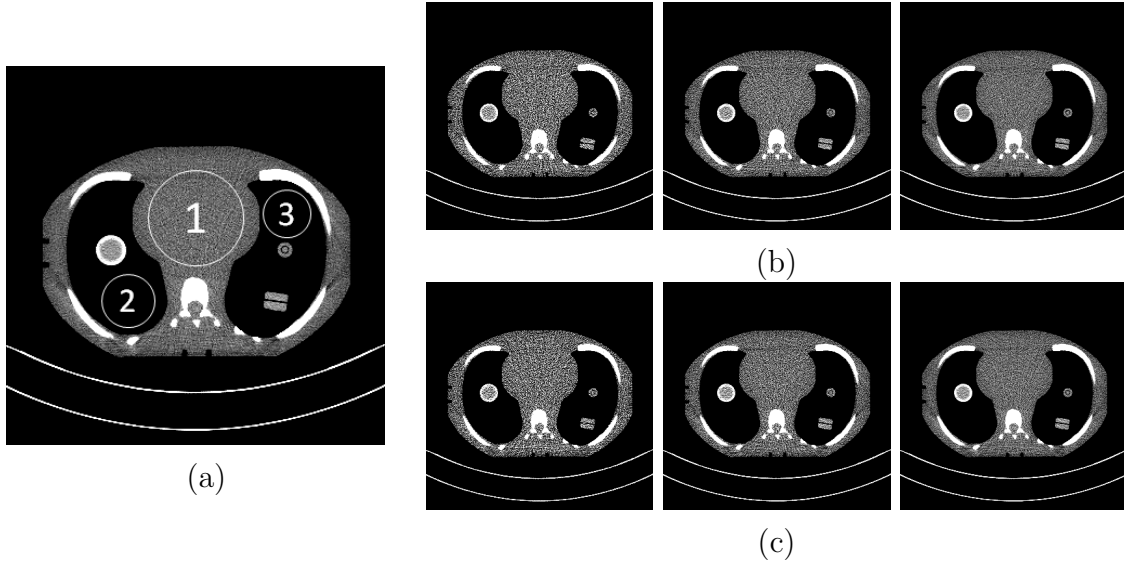


Figure 10: Presentation of (a) the measured high-dose image of 300 mAs, (b) corresponding acquired lower-dose images, and (c) simulated lower-dose images of 20, 50, and 100 mAs (from left to right) using the final model for the sequential scan of the thorax phantom. (window level: 0 HU, window width: 200 HU).

In clinical applications, automatic tube current modulation is widely used to adjust the X-ray tube current for each projection angle which results in a significant dose reduction to the patient. The tube current at each projection angle depends on the size and the different densities of the tissues, therefore, in order to get the same tube current profile for repeated scans the tube angle and the bed position should be exactly the same for all scans. The proposed framework was expanded to simulate the lower-dose helical scans with AEC. The tube current of lower-dose scan was estimated according to the tube current of higher dose scan and nominal tube current as follows

$$\text{tube current}_{low} = \frac{\text{nominal tube current}_{low}}{\text{nominal tube current}_{high}} * \text{tube current}_{high} \quad (23)$$

Using the same anthropomorphic thorax phantom, the experiment was repeated by doing a helical CT scan with AEC. The tube current of the high-dose scan was extracted from the header and the corresponding lower-dose tube current was estimated by Eq. 23. The high-dose scan of 274 effective mAs was used as the input high dose scan (effective mAs is a parameter setting on Siemens CT scanner defined as the product of tube current and rotation time divided by the beam pitch (Massoumzadeh et al. 2009)). The simulation procedure was the same for helical and sequential scans. Fig. 11 represents the noise value of the simulated and the acquired scans for different regions at different levels of tube current. The main problem in scans with AEC is that the profile of tube current is not the same for repeated scans due to the difference in the position of tube in each scan. In addition, the behavior of the system is not the same for high and low dose scans. This misalignment results in a larger error in the simulation of lower dose helical scans compared to the sequential one. Table 4 reports the standard deviation from uniform ROIs in the reconstructions from the helical scan of the anthropomorphic

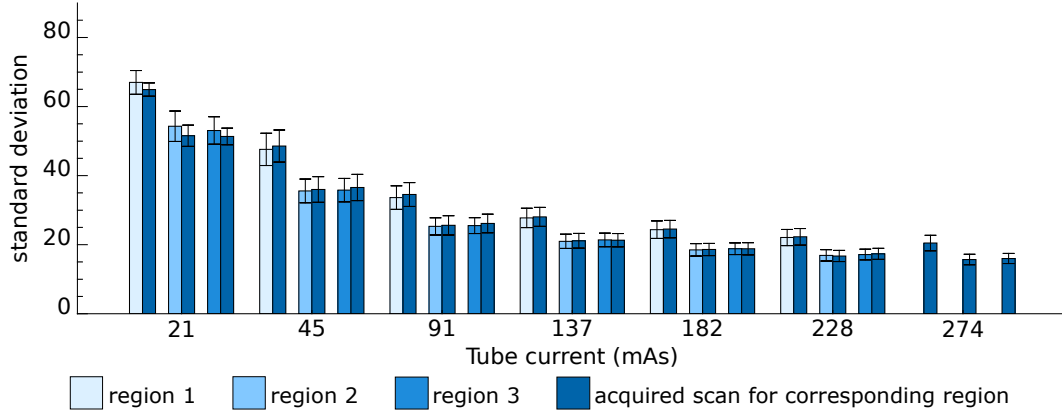


Figure 11: Representation of the noise level in the simulation of the lower-dose helical scan of the anthropomorphic thorax phantom with AEC.

Table 4: Comparison of the noise level in the reconstruction of lower-dose images at different levels of tube current for anthropomorphic abdomen phantom.

Tube current	region 1			region 2			region 3		
	real	sim	error	real	sim	error	real	sim	error
300	20.47	-	-	15.70	-	-	16.00	-	-
250	22.28	22.07	0.9%	16.72	16.91	1.1%	17.35	17.14	1.2%
200	24.52	24.33	0.7%	18.60	18.51	0.5%	18.81	18.83	0.1%
150	28.06	27.75	1.1%	21.13	20.97	0.7%	21.30	21.38	0.3%
100	34.53	33.63	2.6%	25.60	25.30	1.1%	26.14	25.53	2.3%
50	48.57	47.61	1.9%	36.00	35.57	1.1%	36.56	35.80	2.0%
20	64.93	66.99	3.1%	51.56	54.31	5.3%	51.35	53.08	3.3%

thorax phantom. Even though the relative error has slightly increased, the error is less than 5.3%, confirming good performance of the proposed model for helical CT scanning with AEC.

An anthropomorphic abdomen phantom (CIRS E2E SBRT) was also performed to mimic abdominal CT scans. The high dose scan of 300 mAs was used for the simulation. The MLTR (8 iterations and 40 subiterations) was used for the reconstruction. For the comparison, three uniform regions were selected, represented in Fig. 12(a). Table 5 reports the standard deviation of the noise in the simulated and the acquired images at different levels of tube current for each region. Fig. 12 shows the simulated images and corresponding lower dose acquired images.

In order to improve the clinical relevance of the experiments, a realistic CIRS head phantom (Proton Therapy Dosimetry Head, Model 731-HN) was scanned with a routine clinical protocol [helical, AEC, Pitch: 0.55]. The high-dose scan of 192 effective mAs was used as the input high-dose scan to simulate the lower-dose scans. Subsequently, the simulated scans were transferred into the scanner and reconstructed by the scanner's reconstruction software [Kernel: Hr38, Iterative, Strength: 3]. Table 6 compares the

Table 5: Comparison of the noise level in the reconstruction of lower-dose images at different levels of tube current for the sequential scan of the anthropomorphic abdomen phantom.

Tube current	region 1			region 2			region 3		
	real	sim	error	real	sim	error	real	sim	error
300	11.50	-	-	12.36	-	-	12.69	-	-
250	12.44	12.51	0.5%	13.38	13.30	0.6%	13.23	13.30	0.4%
200	13.99	13.96	0.2%	14.67	14.66	0.1%	14.06	14.17	0.8%
150	16.07	16.12	0.3%	16.81	16.74	0.4%	15.42	15.79	2.3%
100	19.77	19.50	1.3%	19.92	19.91	0.0%	17.86	18.36	2.7%
50	26.73	26.80	0.2%	27.00	27.28	1.0%	23.76	24.67	3.8%
20	35.93	36.93	3.3%	35.82	37.12	3.6%	34.66	35.32	1.8%

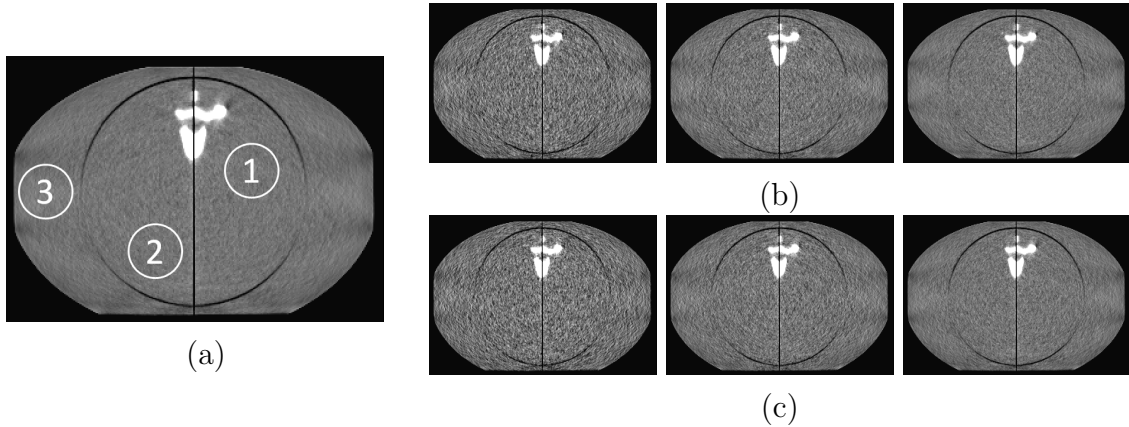


Figure 12: Presentation of (a) the high-dose image of 300 mAs, (b) corresponding acquired lower-dose images, and (c) simulated lower-dose images of 20, 50, and 100 mAs (from left to right) using the final model for the sequential scan of the abdomen phantom. (window level: 0 HU, window width: 300 HU).

noise standard deviation in a uniform region in images obtained from the simulated and acquired scans. For instance, the relative error is 3.2% for the simulation of low-dose scan of 24 effective mAs where the tube current reduced to 12.5% of the normal tube current. Accordingly, the standard deviation of the predicted noise is slightly less than the measured one. Comparing the tube current of measured and simulated scans, it appeared that the level of tube current in the simulated scan is higher than the measured one and consequently a smaller noise level in the simulated images is expected. This misalignment is mainly due to dissimilar behavior of the system for high and low dose scans. Fig. 13 compares the tube current of the estimated and the measured lower-dose scan of 24 effective mAs.

The NPS was also computed for a 61×61 voxel uniform ROI in 32 slices, indicated in Fig. 15(a), to compare the noise texture in the acquired and simulated scans. Fig. 14 compares the NPS of the acquired and simulated scans. As mentioned earlier, the standard deviation of the noise in the simulation of lower dose scan of 24 and 47 mAs is underestimated due to misalignment in the tube current, which results in a higher

Table 6: The detailed comparison of noise levels in the measured and the simulated lower-dose images at different levels of tube current for realistic CIRS head phantom.

Tube current	real	sim	error
192	3.39	-	-
140	3.92	3.91	0.2%
117	4.23	4.24	0.2%
93	4.79	4.69	2.2%
70	5.47	5.44	0.5%
47	6.77	6.65	3.0%
24	9.52	9.21	3.2%

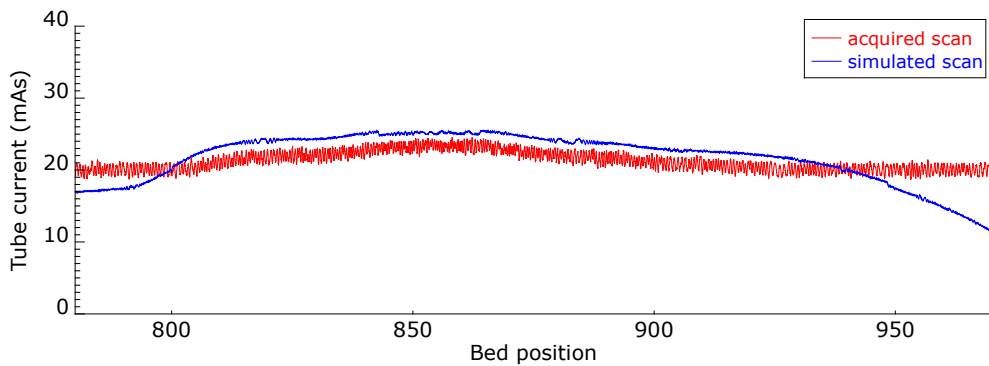


Figure 13: Illustration of the measured and the estimated lower-dose tube current of a helical scan at different projection angle. It is clearly seen that the tube current of the simulated scan is higher than the measured one and therefore the standard deviation of the simulated images would be less than the acquired scan.

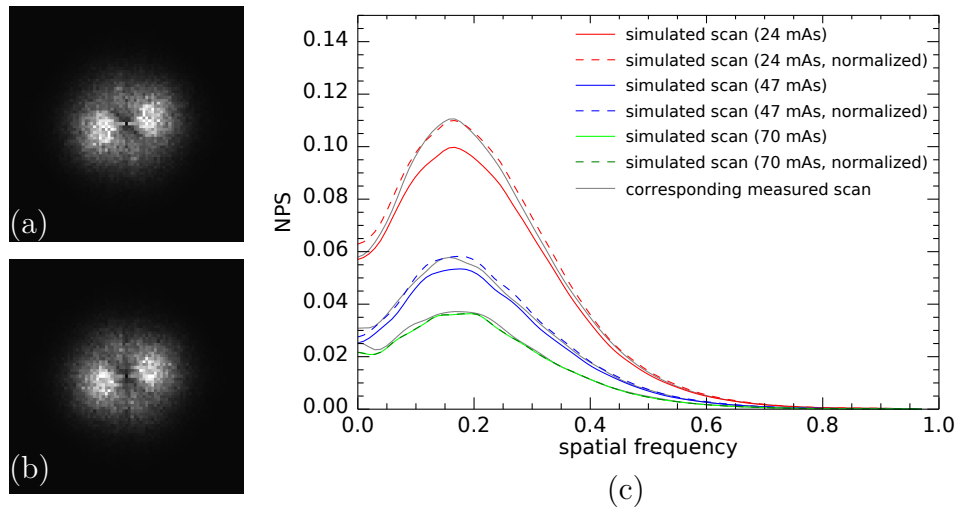


Figure 14: The illustration of the 2D NPS of (a) the measured and (b) the simulated scan of 24 mAs. (c) The comparison of the radially averaged NPS for the measured and the simulated scans of 24, 47, 70 mAs.

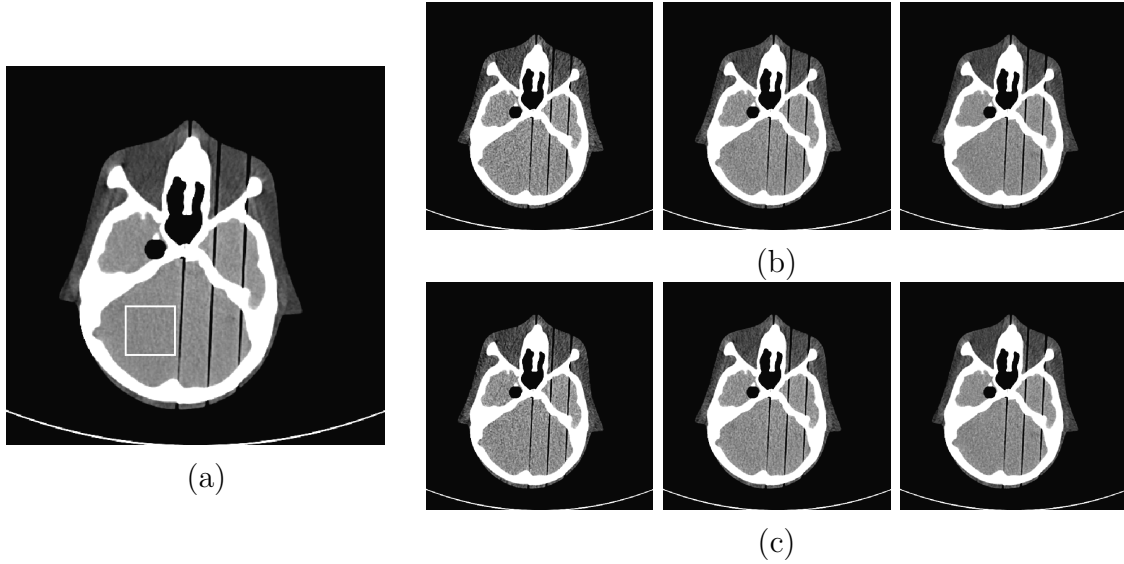


Figure 15: Presentation of (a) the measured high-dose image of 192 effective mAs and (b) corresponding acquired and (c) simulated lower-dose images of 24, 47, and 70 effective mAs (from left to right) using the proposed framework. The square in (a) indicates ROI that was used to compute the NPS in Fig. 14. (window level: 60 HU, window width: 120 HU).

amplitude of NPS for the acquired scans. Therefore, the radially averaged NPS in Fig. 14 was normalized to compare the shape of the 1D NPS in the acquired and simulated scans. Comparing the NPS in Fig. 14 shows a good agreement between the real and the simulated noise which validates the accuracy of proposed model. Fig. 15 shows the high-dose scan of 192 mAs and its corresponding measured and simulated lower-dose scans.

4. Discussion

In this study, a new strategy was proposed to simulate the lower-dose CT scan from an existing standard-dose scan which can be used to optimize CT acquisition protocols. The main application of the developed tool is to determine the lowest exposure scan which still produces sufficient information for the clinical task.

The developed tool simulated lower-dose scans by adding synthetic noise to a high-dose scan in the projection domain which requires access to raw sinogram data. The general idea was to estimate the noise equivalent number of photons in the high dose scan and apply a thinning technique to simulate the lower dose scan. The transmitted signal was considered as the combination of a Poisson and a zero-mean normal distribution to represent the effect of the quantum and electronic noise. The proposed framework accounts for the bowtie filter, for correlated noise between neighboring detector elements, for the beam hardening effect, and for the non-linear smoothing filter. Employing a binomial distribution for thinning accounted for noise in the high dose scan. The main difference with most existing procedures is the modeling of the noise correlation.

It was important to include this correlation in the simulation procedure because the noise propagation through the image reconstruction is not the same for correlated and uncorrelated noise. The experiments revealed that the correlated noise introduced higher noise in the image space for the same noise variance in the sinogram domain. The signal dependent filter was also included in the simulation procedure. Before applying the SDF, the level of the predicted noise was more than the measured one for very noisy data, however, including SDF in the simulation mitigated that.

All the experiments have been performed on Siemens Force scanner, however, the model can be extended for other scanners after appropriate calibration of $I_0^{(1)}$, electronic noise, and correlation matrix of neighboring detector elements. In this study, tube current reduction, without changing any other acquisition parameters (fixed kVp, rotation time, and collimation), was modeled and the tube voltage was set at 120 kVp in all experiments. Any change in acquisition parameters may affect the signal properties and therefore the parameters should be calibrated accordingly.

Different phantom studies with different acquisition protocols were used to evaluate the accuracy of the proposed framework. The results demonstrated excellent accuracy in providing realistic lower-dose images where the texture and magnitude of the simulated noise matched the measurements in both image and projection domains. The standard deviation of the reconstructed image in uniform ROIs revealed a close agreement of the noise level in the observed and simulated lower-dose scans where the relative error was on the order of $\sim 1\%$ for sequential and $\sim 3\%$ for helical scans. For instance, the relative error in the simulation of the low-dose scan of 20 mAs, where the tube current was reduced to 6.6% of the normal tube current, was 1.0% and 0.7% for water and anthropomorphic thorax phantom, respectively. The local NPS of reconstructed images demonstrated a strong agreement between the real and simulated noise. Comparison of the noise level in the sinogram domain also confirmed the good performance of the proposed model.

Sequential and helical scans with/without automatic exposure control can be simulated using the proposed framework. However, the overall error in the simulation of helical scans was increased compared with sequential scans due to the deviations of the tube current modulation. In other words, the behavior of tube current modulation was not the same for low and high dose scans and this dissimilarity introduced an additional error in the simulated lower-dose scans, but we consider the results still acceptable for the optimization of CT scan protocols.

In summary, the proposed lower-dose simulation model can be used to optimize CT acquisition protocols to decrease the radiation dose to the patients. Our main motivation is to determine the lowest possible X-ray CT radiation dose that still produces sufficient information for proton therapy treatment planning, which is the subject of ongoing research.

Acknowledgments

This project is supported by Fonds Baillet-Latour. The authors would like to warmly thank Edmond Sterpin and Xavier Geets for the initial design of the research, Walter Coudyzer and Koen Salvo for their contribution in data collection, and Karl Stierstorfer and Frederic Noo for their valuable comments and suggestions.

References

- Abadi E, Harrawood B, Sharma S, Kapadia A, Segars W P & Samei E 2018 Dukesim: A realistic, rapid, and scanner-specific simulation framework in computed tomography *IEEE transactions on medical imaging* **38**(6), 1457–1465.
- Amir O, Braunstein D & Altman A 2003 Dose optimization tool in ‘Medical Imaging 2003: Visualization, Image-Guided Procedures, and Display’ Vol. 5029 International Society for Optics and Photonics pp. 815–822.
- Benson T M & De Man B K 2010 Synthetic ct noise emulation in the raw data domain in ‘IEEE Nuclear Science Symposium & Medical Imaging Conference’ IEEE pp. 3169–3171.
- Cros M, Joemai R M, Geleijns J, Molina D & Salvadó M 2017 Simdosect: dose reporting software based on monte carlo simulation for a 320 detector-row cone-beam ct scanner and icrp computational adult phantoms *Physics in Medicine & Biology* **62**(15), 6304.
- Elbakri I A & Fessler J A 2003 Efficient and accurate likelihood for iterative image reconstruction in x-ray computed tomography in ‘Medical Imaging 2003: Image Processing’ Vol. 5032 International Society for Optics and Photonics pp. 1839–1851.
- Elhamiasl M & Nuyts J 2019 Simulating lower-dose scans from an available ct scan in ‘15th International Meeting on Fully Three-Dimensional Image Reconstruction in Radiology and Nuclear Medicine’ Vol. 11072 International Society for Optics and Photonics p. 110720X.
- Flohr T, Stierstorfer K, Raupach R, Ulzheimer S & Bruder H 2004 Performance evaluation of a 64-slice ct system with z-flying focal spot in ‘RöFo-Fortschritte auf dem Gebiet der Röntgenstrahlen und der bildgebenden Verfahren’ Vol. 176 © Georg Thieme Verlag KG Stuttgart· New York pp. 1803–1810.
- Flohr T, Stierstorfer K, Ulzheimer S, Bruder H, Primak A & McCollough C H 2005 Image reconstruction and image quality evaluation for a 64-slice ct scanner with-flying focal spot *Medical physics* **32**(8), 2536–2547.
- Frush D P, Slack C C, Hollingsworth C L, Bisset G S, Donnelly L F, Hsieh J, Lavin-Wensell T & Mayo J R 2002 Computer-simulated radiation dose reduction for abdominal multidetector ct of pediatric patients *American Journal of Roentgenology* **179**(5), 1107–1113.
- Guimarães L S, Fletcher J G, Harmsen W S, Yu L, Siddiki H, Melton Z, Huprich J E, Hough D, Hartman R & McCollough C H 2010 Appropriate patient selection at abdominal dual-energy ct using 80 kv: relationship between patient size, image noise, and image quality *Radiology* **257**(3), 732–742.
- Kachelrieß M, Knaup M, Penzel C & Kalender W A 2006 Flying focal spot (ffs) in cone-beam ct *IEEE transactions on nuclear science* **53**(3), 1238–1247.
- Kim C W & Kim J H 2012 Application of ct simulation technique for virtual ultra-low-dose trial in ct colonography in ‘International MICCAI Workshop on Computational and Clinical Challenges in Abdominal Imaging’ Springer pp. 49–57.
- La Riviere P J 2005 Penalized-likelihood sinogram smoothing for low-dose ct *Medical physics* **32**(6Part1), 1676–1683.
- Ma J, Liang Z, Fan Y, Liu Y, Huang J, Chen W & Lu H 2012 Variance analysis of x-ray ct sinograms in the presence of electronic noise background *Medical physics* **39**(7Part1), 4051–4065.

- Massoumzadeh P, Don S, Hildebolt C F, Bae K T & Whiting B R 2009 Validation of ct dose-reduction simulation *Medical physics* **36**(1), 174–189.
- Massoumzadeh P, Earl O A & Whiting B R 2005 Noise simulation in x-ray ct in ‘Medical Imaging 2005: Physics of Medical Imaging’ Vol. 5745 International Society for Optics and Photonics pp. 898–910.
- Mayo J R, Whittall K P, Leung A N, Hartman T E, Park C S, Primack S L, Chambers G K, Limkeman M K, Toth T L & Fox S H 1997 Simulated dose reduction in conventional chest ct: validation study. *Radiology* **202**(2), 453–457.
- Mittone A, Bravin A & Coan P 2014 Radiation dose in breast ct imaging with monochromatic x-rays: simulation study of the influence of energy, composition and thickness *Physics in Medicine & Biology* **59**(9), 2199.
- Naziroglu R E, van Ravesteijn V F, van Vliet L J, Streekstra G J & Vos F M 2017 Simulation of scanner- and patient-specific low-dose ct imaging from existing ct images *Physica Medica* **36**, 12–23.
- Neverauskiene A, Maciusovic M, Burkanas M, Griciene B, Petkevicius L, Zaleckas L, Tamosiunas A & Venius J 2018 Image based simulation of the low dose computed tomography images suggests 13 mas 120 kv suitability for non-syndromic craniostenosis diagnosis without iterative reconstruction algorithms *European journal of radiology* **105**, 168–174.
- Nuyts J, De Man B, Fessler J A, Zbijewski W & Beekman F J 2013 Modelling the physics in the iterative reconstruction for transmission computed tomography *Physics in Medicine & Biology* **58**(12), R63.
- Rong J, Gao P, Liu W, Zhang Y, Liu T & Lu H 2017 Computer simulation of low-dose ct with clinical lung image database: a preliminary study in ‘Medical Imaging 2017: Physics of Medical Imaging’ Vol. 10132 International Society for Optics and Photonics p. 101322U.
- Singh S, Kalra M K, Moore M A, Shailam R, Liu B, Toth T L, Grant E & Westra S J 2009 Dose reduction and compliance with pediatric ct protocols adapted to patient size, clinical indication, and number of prior studies *Radiology* **252**(1), 200–208.
- Sollmann N, Mei K, Hedderich D M, Maegerlein C, Kopp F K, Löffler M T, Zimmer C, Rummeny E J, Kirschke J S, Baum T et al. 2019 Multi-detector ct imaging: impact of virtual tube current reduction and sparse sampling on detection of vertebral fractures *European radiology* pp. 1–11.
- Strother S, Casey M & Hoffman E 1990 Measuring pet scanner sensitivity: relating countrates to image signal-to-noise ratios using noise equivalents counts *Ieee transactions on nuclear science* **37**(2), 783–788.
- Takenaga T, Katsuragawa S, Goto M, Hatemura M, Uchiyama Y & Shiraishi J 2016 A computer simulation method for low-dose ct images by use of real high-dose images: a phantom study *Radiological physics and technology* **9**(1), 44–52.
- Van Slambrouck K & Nuyts J 2012 Metal artifact reduction in computed tomography using local models in an image block-iterative scheme *Medical physics* **39**(11), 7080–7093.
- Wang A S, Feng C & Pelc N J 2012 Image-based synthetic ct: simulating arbitrary low dose single and dual energy protocols from dual energy images in ‘Medical Imaging 2012: Physics of Medical Imaging’ Vol. 8313 International Society for Optics and Photonics p. 83131G.
- Wang A S & Pelc N J 2011a Synthetic ct: Simulating arbitrary low dose single and dual energy protocols in ‘Medical Imaging 2011: Physics of Medical Imaging’ Vol. 7961 International Society for Optics and Photonics p. 79611R.
- Wang A S & Pelc N J 2011b Synthetic ct: Simulating low dose single and dual energy protocols from a dual energy scan *Medical physics* **38**(10), 5551–5562.
- Wang A S, Stayman J W, Otake Y, Vogt S, Kleinszig G, Khanna A J, Gallia G L & Siewerssen J H 2014 Low-dose preview for patient-specific, task-specific technique selection in cone-beam ct *Medical physics* **41**(7), 071915.
- Wang J, Lu H, Liang Z, Eremina D, Zhang G, Wang S, Chen J & Manzione J 2008 An experimental study on the noise properties of x-ray ct sinogram data in radon space *Physics in Medicine & Biology* **53**(12), 3327.

- Whiting B R 2002 Signal statistics in x-ray computed tomography in 'Medical Imaging 2002: Physics of Medical Imaging' Vol. 4682 International Society for Optics and Photonics pp. 53–61.
- Whiting B R, Massoumzadeh P, Earl O A, O'Sullivan J A, Snyder D L & Williamson J F 2006 Properties of preprocessed sinogram data in x-ray computed tomography *Medical physics* **33**(9), 3290–3303.
- Willemink M J, Persson M, Pourmorteza A, Pelc N J & Fleischmann D 2018 Photon-counting ct: technical principles and clinical prospects *Radiology* **289**(2), 293–312.
- Won Kim C & Kim J H 2014 Realistic simulation of reduced-dose ct with noise modeling and sinogram synthesis using dicom ct images *Medical physics* **41**(1).
- Yavuz M & Fessler J A 1998 Statistical image reconstruction methods for randoms-precorrected pet scans *Medical Image Analysis* **2**(4), 369–378.
- Yu L, Shiung M, Jondal D & McCollough C H 2012 Development and validation of a practical lower-dose-simulation tool for optimizing computed tomography scan protocols *Journal of computer assisted tomography* **36**(4), 477–487.
- Žabić S, Wang Q, Morton T & Brown K M 2013 A low dose simulation tool for ct systems with energy integrating detectors *Medical physics* **40**(3).
- Zeng D, Huang J, Bian Z, Niu S, Zhang H, Feng Q, Liang Z & Ma J 2015 A simple low-dose x-ray ct simulation from high-dose scan *IEEE transactions on nuclear science* **62**(5), 2226–2233.